Materials Horizons

ROYAL SOCIETY OF CHEMISTRY

COMMUNICATION

View Article Online
View Journal | View Issue

Cite this: *Mater. Horiz.*, 2023, 10, 4278

Received 3rd April 2023,
Accepted 5th June 2023

DOI: 10.1039/d3mh00503h

rsc.li/materials-horizons

Charge–orbital synergistic engineering of TM@$Ti_3C_2O_{1-x}B_x$ for highly selective CO_2 electrochemical reduction†

Jiahe Peng,[ab] Zuhao Shi,[ab] Jizhou Jiang,[c] Peng Zhang,[d] Jyh-Ping Hsu[e] and Neng Li*[abc]

Inspired by MXene nanosheets and their regulation of surface functional groups, a series of Ti_3C_2-MXene-based single TM atom electrocatalysts with a doped boron (B) atom (TM@$Ti_3C_2O_{2-x}B_x$, TM is V, Cr, Mn, Fe, Co or Ni, x = 0.11) are proposed for achieving a high performance catalytic CO_2 reduction reaction (CO_2RR). The results reveal that the doped B atom involves in the adsorption reaction of CO_2 molecules and CO intermediates in the CO_2RR. The TM-to-C and B-to-C π-back bonding contribute to the activation of the CO_2 molecules and CO intermediates in the CO_2RR. Enough electrons from the single TM atom and B atom occupied orbitals can be injected into the CO_2 molecules and *CO intermediates through direct bonding interactions, which effectively alleviates the difficulty of the first hydrogenation reaction step and further helps CO reduction towards CH_4. The calculated values of ΔG for the first hydrogenation reaction and the formation of *CHO on $Ti_3C_2O_{2-x}B_x$ are significantly smaller than those of other single-atom catalysts (SACs). Fe@$Ti_3C_2O_{2-x}B_x$ is found to have the highest electrocatalytic activity with a limiting potential of ~0.40 V and exhibits a high selectivity for obtaining CH_4 through the CO_2RR compared with the hydrogen evolution reaction. This work is expected to open a research path for engineering the charge–orbital state of the innate atoms of a substrate based on mechanistic insights, which guides the rational design of highly selective MXene-based CO_2RR electrocatalysts.

New concepts

Although the development of efficient atomic electrocatalysts to resolve activity and selectivity issues of the CO_2 reduction reaction (CO_2RR) continues to receive increasing attention, it is still challenging. Most of the previous works in this field have primarily focused on TM atoms and introducing a nonmetal atom to modulate the interplay between the TM active centers and multiple intermediates. Herein, we propose a novel mechanism of introducing a boron element, which takes the advantage of charge–orbital synergism to activate the TM atoms of dual atomic electrocatalysts for the CO_2RR. The charge and orbital order controlling resulting from the combined effect of the single TM atoms and B atom can effectively activate CO_2 molecules and CO intermediates in the CO_2RR process. The TM-to-C, and B-to-C π-back bonding contribute to the activation of CO_2 molecules and CO intermediates in the CO_2RR. Based on this mechanism, we further design a series of TM atoms supported by a monolayer B-doped $Ti_3C_2O_2$ ($Ti_3C_2O_{2-x}B_x$) for the CO_2RR. Following a comprehensive screening strategy, Fe@$Ti_3C_2O_{2-x}B_x$ are identified as promising catalysts with high activity and selectivity. Moreover, we identify the valence states of TM as a valid descriptor to evaluate the CO_2RR performance on such catalysts, realizing a fast pre-screening of other potential dopants on the MXene-based CO_2RR SACs. Our work thus provides a new direction for the rational design of MXene-based dual atomic electrocatalysts.

1. Introduction

The rapid economic development and urbanization have already caused a sharp increase in the global concentration of carbon dioxide (CO_2).[1,2] The global warming resulting from the excessive consumption of fossil fuels not only poses a serious threat to global economic security but also affects resources, energy, ecology, and food security, among others. It also poses a severe challenge to human survival.[3,4] In an attempt to alleviate the increase in the average global temperature, Paris Climate Change Conference signed the Paris Agreement.[5–7]

[a] State Key Laboratory of Silicate Materials for Architectures, Wuhan University of Technology, Wuhan 430070, China. E-mail: lineng@whut.edu.cn
[b] Shenzhen Research Institute of Wuhan University of Technology, Shenzhen 518000, Guangdong, China
[c] School of Chemistry and Environmental Engineering, School of Environmental Ecology and Biological Engineering, Novel Catalytic Materials of Hubei Engineering Research Center, Wuhan Institute of Technology, Wuhan, 430205, China
[d] State Center for International Cooperation on Designer Low-Carbon & Environmental Materials (CDLCEM), School of Materials Science and Engineering, Zhengzhou University, Zhengzhou 450001, Henan, China
[e] Department of Chemical Engineering, National Taiwan University, Taipei, 10617, China

† Electronic supplementary information (ESI) available. See DOI: https://doi.org/10.1039/d3mh00503h

The electrochemical reduction of CO_2 to produce carbon-based fuels and chemicals has great potential in solving current environmental problems and benefiting the economy of our society.[8,9] However, the high chemical stability of CO_2 making it hard to be activated at high conversion rates and selectivity is a crucial issue.[10,11] In addition, the CO_2RR pathway includes a chemical dehydration step leading to adsorption of CO,[12–14] which may act as a poison blocking the surface and impeding further protonation steps because of the high desorption energy and a further reduction barrier.[15–17]

In recent years, intense research has been carried out to discover efficient, selective and stable cathode catalysts. Copper-based materials have been widely regarded as efficient cathode materials for the CO_2RR, producing diverse products, such as carbon monoxide (CO), formic acid (HCOOH), methanol (CH_3OH), methane (CH_4), ethanol (C_2H_5OH), and ethylene (C_2H_4).[18–20] Intense optimization of the catalyst materials and reaction conditions has resulted in significant progress over the past few years.[21,22] Irabien *et al.* found that the Cu^{II} atoms in the HKUST-1 metal–organic framework ($[Cu_3(\mu_6\text{-}C_9H_3O_6)_2]_n$) can promote the electrocatalytic conversion of CO_2 to alcohols.[23] The subsequent research studies have reported Cu-based bimetallic electrocatalysts through doping other transition metal atoms to further improve the CO_2 conversion performance.[24,25] Therefore, downsizing the metal nanostructures to singly dispersed metal atoms is highly desirable for maximizing the efficiency of catalytically active metal sites. Recently, single-atom catalysts (SACs) containing isolated metal atoms dispersed on solid substrates have attracted significant attention in the field of catalysis.

Single transition metal (TM) atoms anchored on a substrate are widely used as the active sites in the CO_2RR.[26,27] The excellent performance of transition metal-based catalysts can be ascribed to their occupied d orbitals, which can donate electrons to the antibonding orbitals of gas molecules.[28–30] Being a nonmetal element, the boron (B) atom in a molecular catalyst with sp^2 or sp^3 hybridization has exhibited great potential for N_2 fixation.[31–33] The B atom also shows the ability to activate CO_2 molecules in the CO_2RR.[34,35] Tang *et al.* found that the bare edge B on armchair boron nitride nanoribbons is a promising candidate for the catalysis of the CO_2RR.[36] In light of the above discussion, the active center of catalysts could be either a single TM atom coordinated by non-metal atoms or a B center. It can be inferred that if B serves as the coordination atom of TM, the active sites with the presence of both B and TM may provide stronger activation capacity.

The results of our previous study indicated that the combined effect of TM and B can effectively and selectively ameliorate the performance of electrochemical N_2 reduction.[37] Being an isoelectronic body of N_2, CO is likely to be activated owing to the combined effect of TM and B atoms. Liu *et al.* successfully fabricated single atomic Fe sites anchored on B and N co-doped carbon (Fe-SA/BNC), which showed excellent CO_2RR activity, achieving the highest faradaic efficiency of ~94% at −0.7 V compared with RHE.[38] However, there is a lack of an in-depth discussion on the mechanisms of CO_2 activation. A detailed understanding of these mechanisms at the atomic scale is of great importance for clarifying the synergistic effect between TM and B atoms that contributes to the CO_2RR. This is beneficial to developing a suitable catalyst with a high catalytic selectivity for the CO_2RR.

In addition to the active center, the choice of substrate is another significant factor that can influence SACs' performance.[39,40] MXenes (*e.g.*, $Ti_3C_2T_x$, Ti_2CT_x and Mo_2CT_x), having a general formula of $M_{n+1}X_nT_x$ (n = 1 to 4) with M, X, and T_x being the early transition metals, C or N, and the surface functional groups (usually as –O, –OH or –F), respectively,[41,42] have been considered as potential substrates for various applications,[43,44] especially in the field of SACs.[45–47] Compared with other supports (*e.g.*, doped graphene, MoS_2, and g-C_3N_4), MXenes have not only the highest metallic conductivity but also abundant surface functional groups for anchoring firmly single atoms.[48] Recently, MXenes have been widely used as the substrates of SACs for the CO_2RR.[49] Zhao *et al.* have successfully demonstrated that a Pt@$Ti_3C_2T_x$-based SAC could readily capture CO_2 or aniline, yielding value-added amides with a high conversion and selectivity.[50] The subsequent study of Yang *et al.* has produced single atom Cu-immobilized $Ti_3C_2T_x$ for an electrocatalytic CO_2RR to produce methanol with a high faradaic efficiency of 59.1%.[51] However, relevant theoretical analyses of the role of B in the MXene-based SACs' CO_2RR are very limited. The SACs of single atoms fixed on the $Ti_3C_2T_x$ mixed functional group surface have been successfully synthesized experimentally.[52,53]

In particular, the B atom has been successfully introduced into $Ti_3C_2T_x$ to replace the O functional group on its surface[54] and the single Ru atom anchored on the B-doped $Ti_3C_2T_x$ exhibited outstanding performance for the hydrogen evolution reaction (HER).[55] Relevant reported results provide valuable information for studying the synergistic effect of TM and B atoms on the CO_2RR performance of $Ti_3C_2T_x$-based SACs. Our previous theoretical analysis also showed that the CO_2RR performance of MXene-based SACs can be efficiently improved through controlling of functional groups.[56] It suggests that an in-depth study on the performance of the CO_2RR through

Neng Li

Congratulations on the 10th anniversary and best wishes to Materials Horizons. Our first paper was published in Materials Horizons, and then chosen as the outstanding paper in the in 2018, and selected as "highlighting the members of the Materials Horizons Advisory Board" in 2021. The best way to express our gratitude is to continue to interact closely with the community, and report our significant research advances, such as novel materials, and new reaction mechanisms. We are proud to have solid and excellent cooperation with such an esteemed journal. Here's to another decade, we would like to further contribute this esteemed journal.

controlling of MXene-based SACs with a mixed functional group surface is necessary. Therefore, we discuss in this study the feasibility of anchoring low cost 3d single TM (TM is V, Cr, Mn, Fe, Co or Ni) atoms on the $Ti_3C_2T_x$'s surface groups as a mixture of B and O ($Ti_3C_2O_{2-x}B_x$) to explore the synergistic effect of TM and B atoms on $Ti_3C_2T_x$-based SACs for the CO_2RR. The analysis is based on DFT calculations.

As expected, the results of our computation show that the combined effect of single TM atoms and B atom markedly activated CO_2 molecules and CO intermediates after adsorption. This can be attributed to the injection of adequate charge from the occupied p and d orbitals of B and TM, respectively. In addition, the introduction of the B atom into surface groups can significantly enhance the single atom anchoring capacity. The adsorbed CO_2 can be further reduced to CH_4 on the Fe@$Ti_3C_2O_{2-x}B_x$ SAC with a rather low overpotential of 0.40 eV. The stability of TM@$Ti_3C_2O_{2-x}B_x$ is systematically evaluated, and the results obtained reveal that the designed catalyst can be synthesized promisingly.

2. Computational details

All calculations were performed on the Vienna *ab initio* simulation package (VASP).[57] The Perdew–Burke–Ernzerhof (PBE) functional in the generalized gradient approximation (GGA) was used to express electron exchange correlation[58] and a projector augmented wave (PAW) method was applied to describe the pseudo-potentials.[59] Dispersion-corrected DFT-D3 schemes were employed to describe possible van der Waals (VDW) interactions.[60] The energy cut-off for the plane-wave basis was set at 450 eV. All configurations were based on a $3 \times 3 \times 1$ supercell of $Ti_3C_2T_x$ with a vacuum layer larger than 20 Å in the z direction to prevent the interaction between periodic images. The Brillouin zone in reciprocal space was sampled using the Monkhorst–Pack scheme with $5 \times 5 \times 1$ k-point grids for geometry optimization and electronic structure calculations.

All structures were fully relaxed until the forces became smaller than 0.01 eV Å^{-1}; the convergence threshold in electronic relaxation was set at 10^{-5} eV using the conjugate gradient algorithm. The atomic charge was calculated through Bader's charge population analysis.[61] The atomic structures were analyzed using the VESTA code.[62] The effect of water was considered using the VASPsol code.[63–65] The stability of catalysts was evaluated using *ab initio* molecular dynamics (AIMD) simulations carried out by placing MXene in a vacuum or liquid water and lasted for 10.0 ps with a time step of 1 fs in the *NVT* ensemble.

The binding energy (E_b) and cohesive energy (E_c) of the transition metals on $Ti_3C_2T_x$ can be evaluated using

$$E_b = E_{TM-MX} - E_{MX} - E_{TM} \quad (1)$$

$$E_c = E_{(TMbulk)}/N - E_{TM}, \quad (2)$$

where E_{TM-MX}, E_{MX}, and E_{TM} are the total energies of $Ti_3C_2T_x$ with and without transition metals and the isolated transition metals, respectively.[66] $E_{(TMbulk)}$ and N are the energy of the bulk crystal unit cell of the corresponding transition metals and the number of atoms in the unit cell, respectively. The adsorption energy (ΔE_{ad}) of the different intermediates can be calculated using

$$\Delta E_{ad} = E_{X^*} - E_* - E_X, \quad (3)$$

where E_{X^*}, E_*, and E_X represent the energies of the total system after adsorption, the catalyst, and the adsorbates, respectively.[67]

A computational hydrogen electrode (CHE) model proposed by Nørskov *et al.*[68] was used to calculate the Gibbs free energy (G) of the reaction for the CO_2RR elementary steps involving ($H^+ + e^-$) pair transfer. In the CHE model, $H^+ + e^- \rightleftharpoons 1/2H_2$ (g) is in equilibrium with gaseous H_2 at 0 V *vs.* the reversible hydrogen electrode (RHE) for all pH values at 1 bar of H_2 pressure. The Gibbs free energy of each elementary step was calculated at 298.15 K using the following eqn (4):

$$G = E + ZPE + \int C_P dT - TS + G_{pH} \quad (4)$$

where E is the total energy and T is the temperature. ZPE, $\int C_P dT$, and TS are the zero-point energy, the enthalpy changes from 0 to T K contributed by molecular vibrations, and the entropy correction based on the calculated vibrational frequencies, respectively. G_{pH} represents the free energy correction for pH, defined as $G_{pH} = -k_B T \ln[H^+] = k_B T \ln 10 \times pH$, where k_B is the Boltzmann constant.

In this work, the pH value was set at 0 for strongly acidic conditions.[68] The dependence of the potential (U) on the RHE required for each protonation step is expressed as $U = -\Delta G/e$, where ΔG is the free energy change along each CO_2RR pathway. The limiting potential (U_L) was obtained from the maximum $\Delta G(\Delta G_{max})$ of each elementary step. Since the Gibbs free energy of the O_2, CO, and CO_2 molecules in a gas-phase species cannot be calculated precisely using conventional PBE exchange–correlation function,[14,69] the free energy of the experimental thermodynamic data was used as a ref. 70 and 71. The free energy of liquid-phase molecules (H_2O and CH_3OH) was calculated by considering them as an ideal gas and using their corresponding vapor fugacity (f) at $\mu_{(liquid)} = \mu_{(vapor)}$.[14]

3. Results and discussion

3.1. Stability of single atoms embedded on $Ti_3C_2O_{2-x}B_x$

The diffusion and aggregation of the dispersed single atoms on a support can lower the activity and durability of SACs, whereas $Ti_3C_2T_x$ can capture and stabilize the heteroatom effectively through creating tight bonds between the TM atoms and surface groups. In general, the hollow position consisting of three oxygen groups is the main site on pure $Ti_3C_2T_x$ to fix single TM atoms.[72,73] Therefore, we established a pure $Ti_3C_2T_x$ with oxygen groups covering its surface ($Ti_3C_2O_2$). As introduced previously, the B atom can replace the position of the surface oxygen functional group and be used as the coordination atom to fix the TM atom when doped in $Ti_3C_2O_2$ ($Ti_3C_2O_{2-x}B_x$). As shown in Fig. 1a and b, two possible hollow sites (H1 and H2) might present to locate the TM on the surface of $Ti_3C_2O_2$

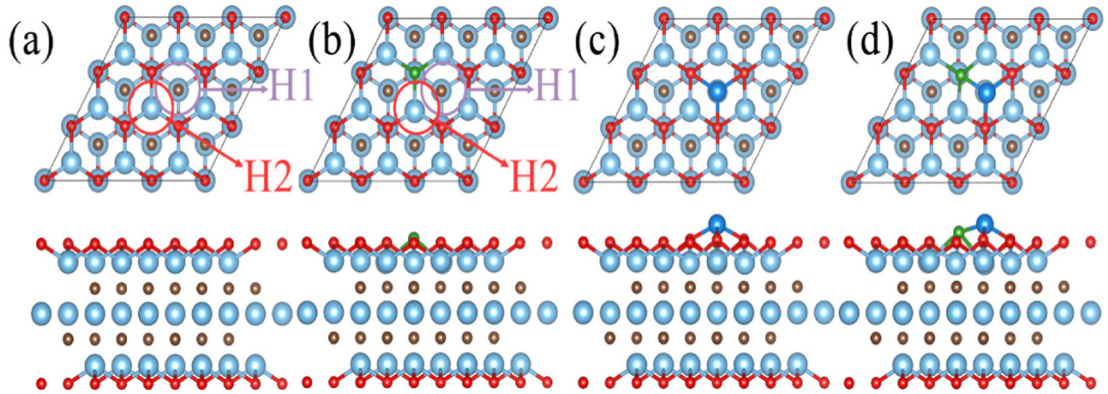

Fig. 1 Optimized models of (a) pure $Ti_3C_2O_2$ and (b) $Ti_3C_2O_{2-x}B_x$; color scheme: Ti, cyan; C, brown; O, red; B, green; and TM, blue. Circles represent the possible sites of TM on $Ti_3C_2O_2$. Optimized structures of (c) pure $Ti_3C_2O_2$ and (d) $Ti_3C_2O_{2-x}B_x$ monolayer confining TM single atoms at the H1 site.

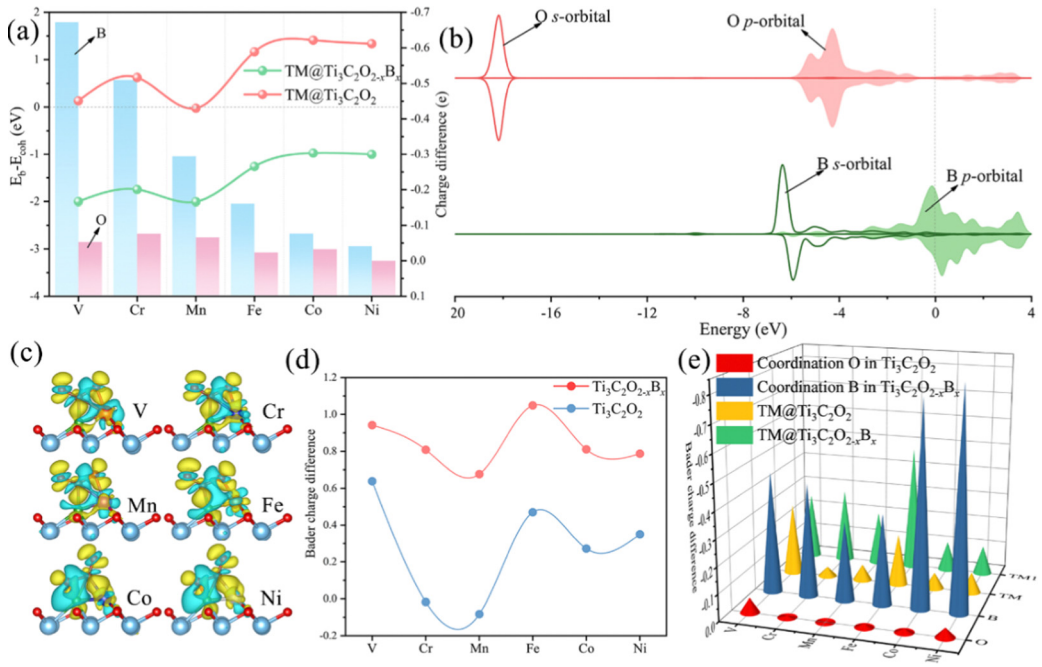

Fig. 2 (a) The E_b–E_{coh} values of TM@$Ti_3C_2O_{2-x}B_x$ and TM@$Ti_3C_2T_x$ (line chart), charge differences of B and O atoms before and after anchoring a single TM atom (histogram). (b) PDOSs (projected density of states) of the O or B surface atoms before fixing the TM single atoms. (c) Variation of charge density differences of TM@$Ti_3C_2O_{2-x}B_x$ with a CO_2 adsorption configuration. The yellow region denotes charge accumulation and the blue region indicates charge depletion, where the isosurface value is set to be 0.03 e Å^{-3}. (d) Bader charge differences of the C atom in CO_2 before and after adsorption on TM@$Ti_3C_2O_{2-x}B_x$ and TM@$Ti_3C_2T_x$. (e) Bader charge differences of TM atoms, the coordination O atom in TM@$Ti_3C_2O_2$ and the coordination B atom in TM@$Ti_3C_2O_{2-x}B_x$ before and after CO_2 adsorption.

and $Ti_3C_2O_{2-x}B_x$. Previous studies, both theoretical and experimental, have identified that the H1 site is a stable adsorption site for metal atoms (Fig. 1c and d).[51,55]

Thermodynamically, the aggregation of the dispersed TM atoms depends on the bond strength between the TM and the substrate as well as the recombination ability of metal atoms. Therefore, the stability of SACs can be measured using the values of E_b–E_{coh} of the TM and substrate (eqn (1) and (2)): the smaller this value the more thermodynamically stable the structure of SACs (Table S1, ESI†). For all of the TM atoms, the value of E_b–E_{coh} for TM@$Ti_3C_2O_{2-x}B_x$ is lower than that for TM@$Ti_3C_2O_2$, suggesting that the presence of B is advantageous for stabilizing TM atoms (Fig. 2a). This can be explained by the fact that B atoms bind TM atoms through substantial partial charge transferred from the latter to the former. When the B atom is doped into the $Ti_3C_2O_2$ substrate, two electrons are transferred from the latter to the former, leaving the partial 2p orbital with lack of electrons. The empty 2p orbital helps the B atom gaining more electrons from the TM single atom than from O atom (Fig. 2a), leading to a thermodynamically more stable structure.

As shown in Fig. 2b, since the localized 2s orbital of the O atom is in the deep energy level, it is difficult for this orbital to

participate in bonding. The 2p orbital of the O atom is almost below the Fermi level, implying that it is fully occupied. The O atom with a saturated electronic structure is not conducive for receiving electrons from TM atoms. Compared with the O atom, the 2s orbital of the B atom is localized in a shallower energy level that is adjacent to its 2p orbital. The 2s orbital of the B atom and the d orbitals of the TM atom have obvious overlaps in the energy level ranging from −6 to 0 eV, indicating intense interactions between the TM and B atoms (Fig. S1, ESI†).

A part of the 2s orbital of the B atom is at the delocalization state and slightly contributes to the electronic state at the Fermi level, demonstrating the hybridization of B s–p orbitals. The partial 2p orbital of the B atom is above the Fermi level and the unoccupied 2p orbital can accept electrons from TM atoms to form strong-polarized covalent TM–B bonds. In addition, we have calculated the area of the H1 site, which is defined as the triangular area enclosed by three oxygen atoms in $Ti_3C_2O_2$ or two oxygen atoms and one boron atom in $Ti_3C_2O_{2-x}B_x$ (Fig. S2, ESI†). The calculated area of the H1 site of $Ti_3C_2O_{2-x}B_x$ (4.21 Å^2) is larger than that of $Ti_3C_2O_2$ (4.11 Å^2). The larger area in the former provides more spacious H1 sites so that TM atoms can be effectively embedded into the flat substrate of $Ti_3C_2O_{2-x}B_x$. Since our results suggest that $Ti_3C_2O_{2-x}B_x$ has an outstanding ability to fix TM single atoms, all the six kinds of metal are considered in the following CO_2RR investigation.

3.2. CO_2 electroreduction reaction on TM@$Ti_3C_2O_{2-x}B_x$ SACs

3.2.1. Initial activation of CO_2. One method of effective activation of CO_2 is changing its linear structure (O═C═O) to a V-shaped ($\angle OCO < 180^\circ$) structure, where partially negatively charged CO_2 is generated due to the injection of electrons into its antibonding $2\pi_u^*$ orbital. As shown in Fig. S3 (ESI†), CO_2 binds to TM@$Ti_3C_2O_{2-x}B_x$ (TM is V, Cr, Mn or Fe) through a B–C–TM–O configuration, but to TM@$Ti_3C_2O_{2-x}B_x$ (TM is Co or Ni) through an O–B–C–TM configuration. The linear O═C═O is bent substantially and its C atom binds to the TM atom and the nearby B atom in both configurations. These bonding configurations indicate that the B atom can participate in the CO_2 adsorption. In the case of TM@$Ti_3C_2O_2$ (Fig. S3, ESI†), CO_2 binds to TM (TM is V, Fe, Co or Ni) through a bidentate C–TM–O configuration with a bent structure, but binds to TM (TM is Cr or Mn) through a monodentate O–M configuration with a linear structure. This reveals that TM@$Ti_3C_2O_2$ (TM is V, Fe, Co or Ni) also has the ability to activate CO_2 molecules. However, for all the TM@$Ti_3C_2O_2$ considered, CO_2 molecules only bind to the TM atom, implying that the O atom of the functional groups does not participate in the CO_2 activation directly. As can be seen in Table 1, the bending angle of the CO_2 adsorbed on TM@$Ti_3C_2O_{2-x}B_x$ is smaller than that on TM@$Ti_3C_2O_2$, suggesting a more significant CO_2 activation in the former.

Table 1 Binding energy (BE), binding distance (BD), and bond angle (BA) of CO_2 adsorbed on TM@$Ti_3C_2O_{2-x}B_x$ and TM@$Ti_3C_2O_2$ in the most stable configuration

	$Ti_3C_2O_{2-x}B_x$				$Ti_3C_2O_2$		
	BE	BD (Å)		BA	BE	BD (Å)	BA
Metal	(eV)	TM–C	B–C	($\angle$OCO, °)	(eV)	TM–C	($\angle$OCO, °)
V	−1.49	2.12	1.72	128.7	−0.62	2.01	140.7
Cr	−1.03	2.10	1.74	130.5	−0.65	—	179.7
Mn	−0.52	2.15	1.81	136.5	−0.48	—	179.4
Fe	−0.73	2.48	1.62	126.5	−0.27	2.06	151.9
Co	−1.34	1.86	1.82	125.3	−0.09	2.09	158.9
Ni	−1.62	1.89	1.82	126.8	−0.25	1.98	153.5

These phenomena we discussed above indicate that the doping of B facilitates the activation of CO_2 through participating in its adsorption process. To understand the emerging role of the B atom in CO_2 activation, we examine the electronic structures of TM@$Ti_3C_2O_{2-x}B_x$ and TM@$Ti_3C_2O_2$ through a Bader charge analysis. The images of the charge density difference of the CO_2 adsorbed TM@$Ti_3C_2O_{2-x}B_x$ are shown in Fig. 2c. As seen, charge accumulated in the CO_2 $2\pi_u^*$ antibonding orbital around the C atom, leading to the activation of CO_2 molecules. In contrast, charge depleted around B and TM atoms, confirming that the electrons involved in the activation of CO_2 come from these atoms. To give more details of charge transfer density, Bader effective charge is investigated. When adsorbed on the surface, the C atom of CO_2 in the case of TM@$Ti_3C_2O_{2-x}B_x$ can gain more electrons than that in the case of TM@$Ti_3C_2O_2$ (Fig. 2d).

Generally, the strong electronegativity of oxygen shifts the focus of electronic clouds on both ends of CO_2 molecules, yielding an electron-deficient carbon center. An injection of electron into the C atom is an effective way to activate CO_2 molecules. The observation that TM@$Ti_3C_2O_{2-x}B_x$ has a more activated CO_2 is consistent with the results of calculations. Bader effective charge analysis (Fig. 2e) also shows that B and TM atoms can provide enough electrons for injection into CO_2 molecules. In particular, in the cases of Co@$Ti_3C_2O_{2-x}B_x$ and Ni@$Ti_3C_2O_{2-x}B_x$, most of the injected electrons come from the B atom. When CO_2 molecules are activated on TM@$Ti_3C_2O_2$, the $Ti_3C_2O_2$ substrate can provide extra electrons to activate CO_2, which is consistent with our previous result.[56] But an indirect participation mode provides less electron than a direct participation.

The reaction activity of the doped B atom can be ascribed to its occupied 2p orbitals with s–p hybridization. Because the electronegativity of B is weaker than that of C, the electrons in the occupied orbitals of the B atom can transfer easily to the C atom of the CO_2 molecule. In contrast, the full 2p-orbital occupation electronic structure of the O atom leads to a strong chemical stability. The stronger electronegativity of the O atom also makes it difficult for the C atom to grab its electrons. To gain insights into the chemisorption of CO_2 on the active site of TM@$Ti_3C_2O_{2-x}B_x$, the bonding states of CO_2 on TM@$Ti_3C_2O_{2-x}B_x$ were investigated. According to the projected density of states (PDOS) for an isolated CO_2 molecule (Fig. 3a–d and Fig. S4, ESI†), the empty orbital above the Fermi level is the antibonding $2\pi_u^*$ orbital.

According to the PDOS of bare TM@$Ti_3C_2O_{2-x}B_x$, TM 3d overlaps with B 2p, indicating the bonding of TM and B atoms.

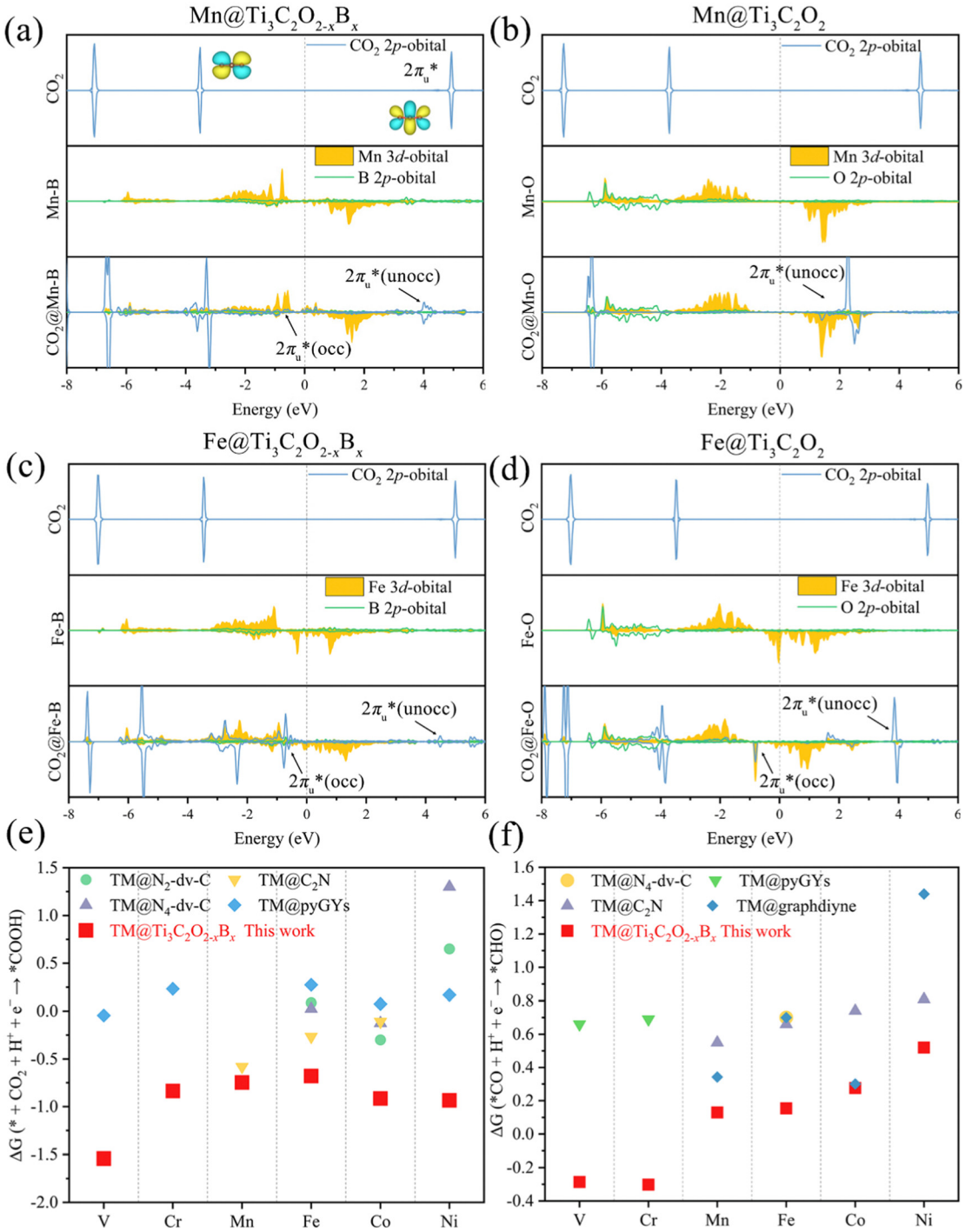

Fig. 3 The PDOS of CO_2 2p, TM 3d, and coordination atoms (the O atom in $TM@Ti_3C_2O_2$ and the B atom in $TM@Ti_3C_2O_{2-x}B_x$) of the 2p orbital before and after CO_2 adsorption on (a) $Mn@Ti_3C_2O_{2-x}B_x$, (b) $Mn@Ti_3C_2O_2$, (c) $Fe@Ti_3C_2O_{2-x}B_x$ and (d) $Fe@Ti_3C_2O_2$. A comparison of the Gibbs free energy changes of (e) the 1st ($CO_2 + H^+ + e^- \rightarrow$ *COOH) and (f) the 3rd ($CO + H^+ + e^- \rightarrow$ *CHO) hydrogenation reactions for $TM@Ti_3C_2O_{2-x}B_x$ and other SACs ($TM@N_2$-dv-C,[74] $TM@N_4$-dv-C,[74] $TM@C_2N$,[75] TM@pyGYs,[76] and TM@graphdiyne[77]) for the CO_2 reduction.

After its adsorption on $TM@Ti_3C_2O_{2-x}B_x$, the antibonding $2\pi_u^*$ of CO_2 splits into two parts: one above and one below the Fermi level. The states above the Fermi level are contributed by the unoccupied TM 3d-CO_2 $2\pi_u^*$ and B 2p-CO_2 $2\pi_u^*$ hybridization orbitals, while the overlapping of occupied TM 3d-CO_2 $2\pi_u^*$ and B 2p-CO_2 $2\pi_u^*$ hybridization orbitals can be found at −2 to 0 eV, just below the Fermi level. After adsorbing on $TM@Ti_3C_2O_2$, the antibonding $2\pi_u^*$ orbital of CO_2 also splits into one part above the Fermi level and one part below it. Notably, the peak intensity of the unoccupied CO_2 $2\pi_u^*$ orbital when CO_2 adsorbed on $TM@Ti_3C_2O_{2-x}B_x$ decreases more sharply than that when CO_2 adsorbed on $TM@Ti_3C_2O_2$. This implies that

$TM@Ti_3C_2O_{2-x}B_x$ provides more electrons that can be injected into the $2\pi_u^*$ orbital, which is consistent with the results of Bader charge analysis.

Besides CO_2 activation ability, another key issue in CO_2RR catalyst design is to obtain an energy-rich product (CH_4), which is closely related to the adsorption Gibbs free energy of radical reaction intermediates and that of the elementary CO_2 reduction reaction. CO_2RR can be differentiated by the types of intermediates formed in the initial protonation steps of CO_2: formate (*OCHO) and carboxyl (*COOH). The calculated Gibbs free energy changes (ΔG) for the formation of *COOH and *OCHO ($*CO_2 + H^+ + e^- \rightarrow$ *COOH or *OCHO) on $TM@Ti_3C_2O_{2-x}B_x$ are summarized in Fig. S5 (ESI†). This figure shows that the 1st hydrogenation (H^+/e^-) reactions are energetically prone to occur on the O atom rather than on the C atom, suggesting that the formation of *COOH is more energetically preferred than that of *OCHO. The calculated ΔG shown in Fig. 3e reveals that the ΔG of the first hydrogenation reaction to form *COOH on $TM@Ti_3C_2O_{2-x}B_x$ is smaller than that in previous studies, illustrating the superior CO_2 activation ability of $TM@Ti_3C_2O_{2-x}B_x$.

3.2.2. Origin of CO activity on $TM@Ti_3C_2O_{2-x}B_x$. According to previous studies, *COOH will always lead to the formation of *CO *via* releasing one H_2O molecule, and further reduce to intermediate *CHO.[14,74,75] Besides *COOH, *CO is another crucial intermediate in the CO_2RR to form CH_4, the adsorption energy of which is closely related to CO_2RR performance. The weak CO adsorption on SACs results in direct desorption of CO under low electrode potentials. Therefore, a stably adsorbed CO on SACs may improve its further reduction towards CH_4.

The relatively higher CO adsorption strength on $TM@Ti_3C_2O_{2-x}B_x$ (Table S2, ESI†) results in poor activity for CO direct desorption under low electrode potentials. Due to the outstanding stability of CO, the hydrogenation reaction needs too much energy to reduce *CO. If the ΔG of the reaction $*CO + H^+ + e^- \rightarrow$ *CHO is larger than that of the reaction $*CO \rightarrow CO + *$, CO is inclined to desorb rather than further hydrogenation. However, a high voltage is still needed to remove *CO from the surface if the adsorption of CO on the catalyst is strong. In general, the lower hydrogenation ΔG of the reaction $*CO + H^+ + e^- \rightarrow$ *CHO is necessary for the further CO reduction process. Therefore, the activation of the *CO intermediate is a key criterion to evaluate the performance of the CO_2RR on SACs.

To verify the performance of $TM@Ti_3C_2O_{2-x}B_x$ in *CO reduction, we calculated the ΔG of the reaction $*CO + H^+ + e^- \rightarrow$ *CHO, along with the ΔG of other SACs. Having examined the available results for the CO_2RR of SACs, we can find that $*CO + H^+ + e^- \rightarrow$ *CHO is the potential-determining step in most of these studies. As shown in Fig. 3f, the calculated ΔG for the reaction $*CO + H^+ + e^- \rightarrow$ *CHO on $TM@Ti_3C_2O_{2-x}B_x$ is smaller than the corresponding values of ΔG reported in previous studies, which verifies the superior CO activation ability of $TM@Ti_3C_2O_{2-x}B_x$. According to the adsorption configuration of *CO on $TM@Ti_3C_2O_{2-x}B_x$, the B atom also participates in the adsorption process (Fig. 4a), demonstrating its important role in CO activation. To gain insights into the combined effect of multi-active site TM and B atoms in ameliorating the CO reduction, the orbital and charge transfer of TM and B atoms during the adsorption of *CO is also investigated. The configuration of the *CO adsorbed on $TM@Ti_3C_2O_2$ is used for comparison.

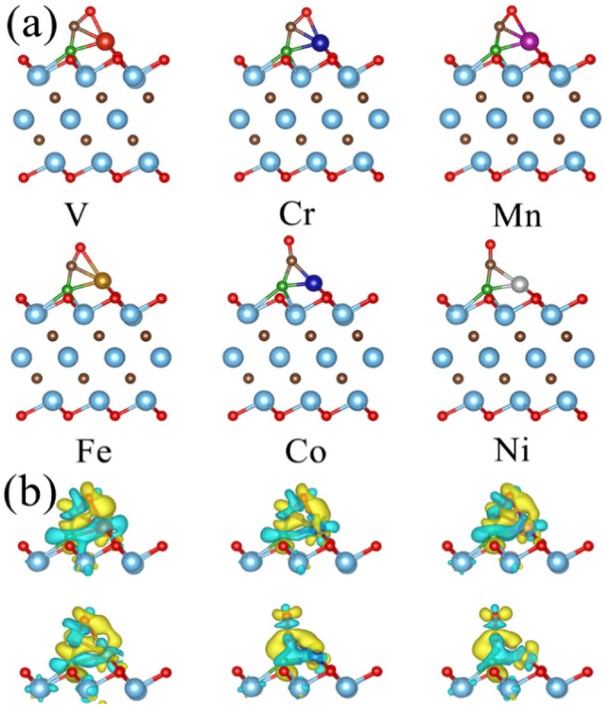

Fig. 4 (a) Optimized geometric structures of CO adsorbed on $TM@Ti_3C_2O_{2-x}B_x$. (b) Variation in the difference of charge density of $TM@Ti_3C_2O_{2-x}B_x$ with a CO adsorption configuration. The yellow region denotes charge accumulation and the blue region indicates charge depletion, where the isosurface value is set to be 0.03 e $Å^{-3}$.

Accepting the lone-pair electrons from the σ_g orbital of CO and donating electrons to the antibonding π_g^* orbitals of CO are the main ways to weaken the C≡O triple bond, known as the "acceptance–donation" process.[78,79] Fig. 4b and Fig. S6 (ESI†) illustrate the calculated charge density differences for the CO adsorption configuration on $TM@Ti_3C_2O_{2-x}B_x$ and $TM@Ti_3C_2O_2$. Charge accumulation and depletion can be observed for both CO molecules and B–TM atoms on $TM@Ti_3C_2O_{2-x}B_x$. This phenomenon is actually in perfect accordance with the "acceptance–donation" process mentioned above. A comparison between the area of the isosurface of CO adsorbed on $TM@Ti_3C_2O_{2-x}B_x$ and that on $TM@Ti_3C_2O_2$ reveals that the charge transfer in the former is more obvious than that in the latter.

To further elucidate the bonding nature, the PDOS of the adsorption of CO on $TM@Ti_3C_2O_{2-x}B_x$ and that on $TM@Ti_3C_2O_2$ are investigated (Fig. 5 and Fig. S7, ESI†). After adsorbing on $TM@Ti_3C_2O_{2-x}B_x$ and $TM@Ti_3C_2O_2$, the σ_g orbital of CO in a deep level obviously splits and moves to deeper energy states, indicating the interaction between the CO σ_g orbital and SACs. It can be seen that a part of the π_g^* orbitals of CO unoccupied (unocc) shifts upward to the Fermi level and the

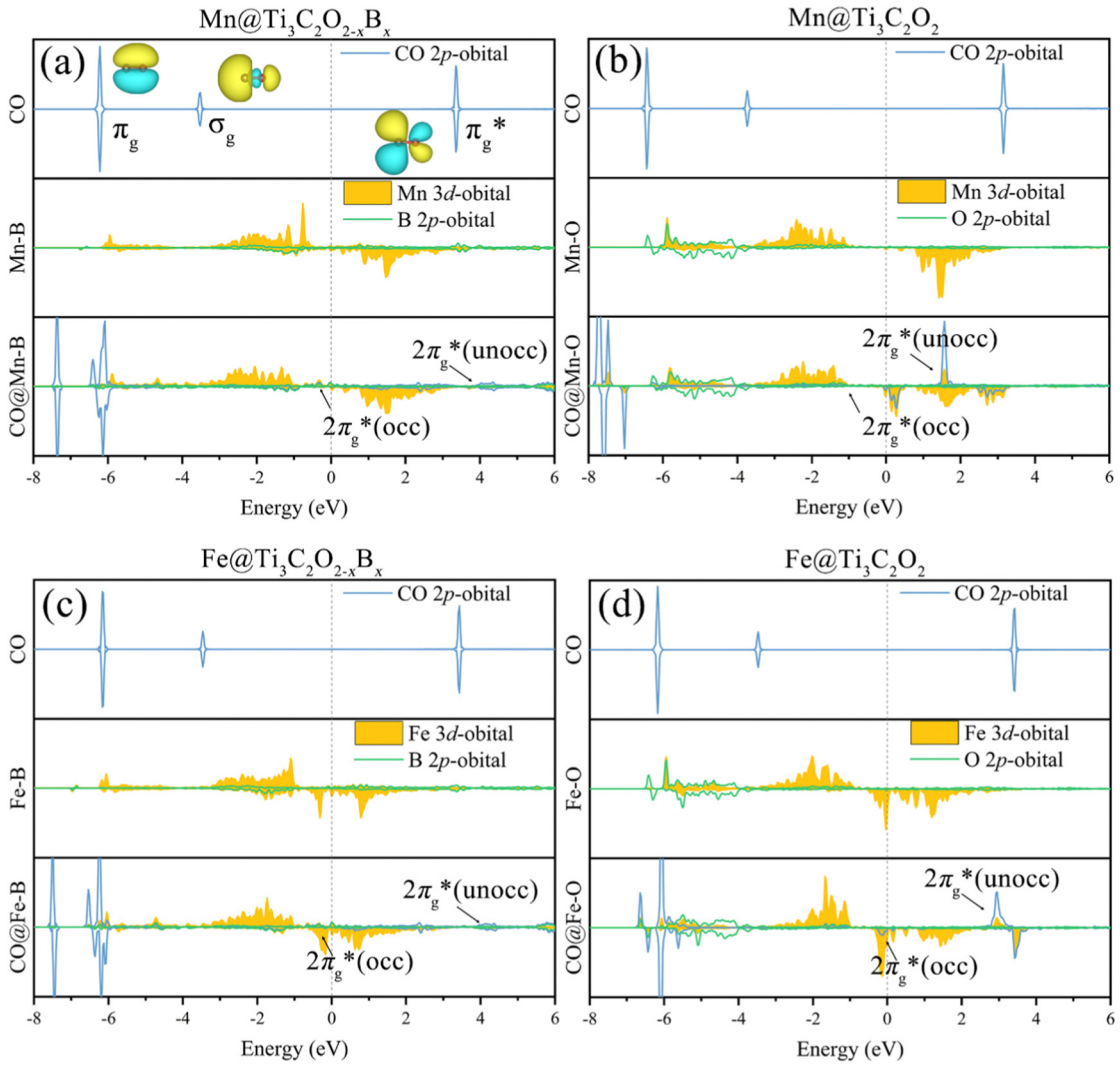

Fig. 5 The PDOS of CO 2p, TM 3d, and coordination atoms (the O atom in TM@$Ti_3C_2O_2$ and the B atom in TM@$Ti_3C_2O_{2-x}B_x$) of the 2p orbital before and after CO_2 adsorption on (a) Mn@$Ti_3C_2O_{2-x}B_x$, (b) Mn@$Ti_3C_2O_2$, (c) Fe@$Ti_3C_2O_{2-x}B_x$ and (d) Fe@$Ti_3C_2O_2$.

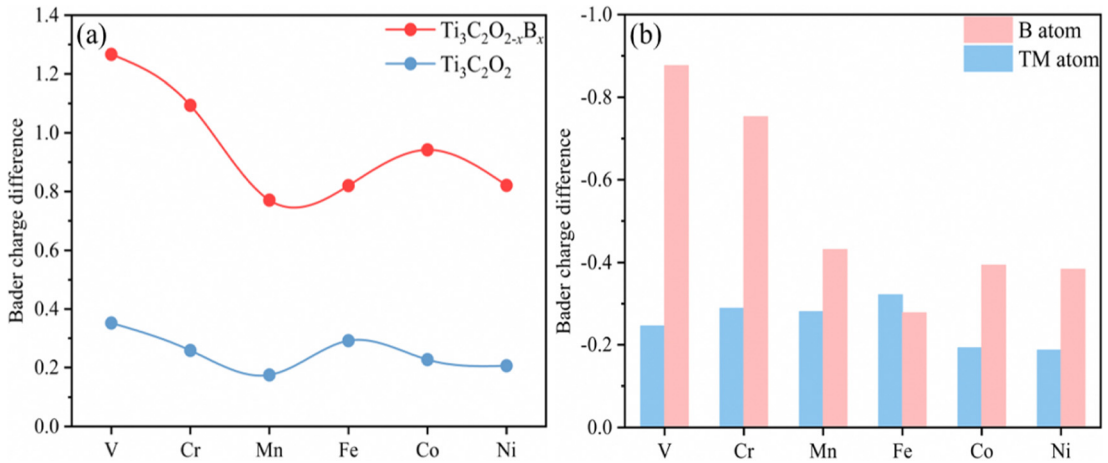

Fig. 6 (a) Bader charge differences of the C atom in CO before and after adsorption on TM@$Ti_3C_2O_{2-x}B_x$ and TM@$Ti_3C_2T_x$. (b) Bader charge differences of TM atoms and the B atom on TM@$Ti_3C_2O_{2-x}B_x$ before and after CO adsorption.

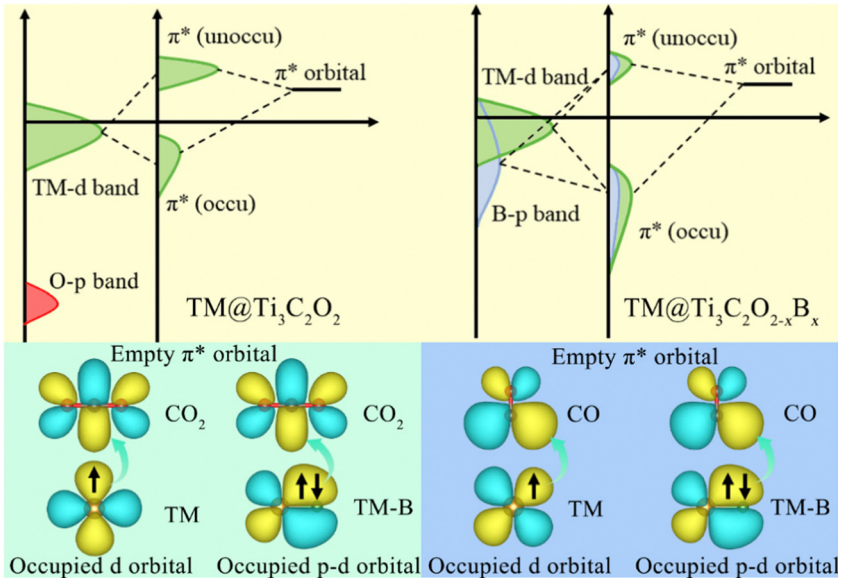

Fig. 7 Schematic diagrams of CO_2 molecule and CO intermediate activation mechanisms on $TM@Ti_3C_2O_2$ and $TM@Ti_3C_2O_{2-x}B_x$.

other part moves downward to the Fermi level near −2 eV to form a π_g^* occupied (occ) orbital. Compared with that of $TM@Ti_3C_2O_2$, the peak intensity of the unoccupied CO π_g^* antibonding orbital decreases more sharply when CO is adsorbed on $TM@Ti_3C_2O_{2-x}B_x$, indicating the better CO activation performance of $TM@Ti_3C_2O_{2-x}B_x$. The Bader charge analysis shows that the C atom from CO can gain more electrons from $TM@Ti_3C_2O_{2-x}B_x$ (Fig. 6a and b), which is consistent with the above PDOS analysis.

Owing to its weak electronegativity and not fully occupied orbital structure, the electrons in the occupied orbitals of the B atom can easily transfer to the empty orbitals of the CO_2 molecule and CO intermediate. Based on the results gathered, it can be reasonably inferred that a combined effect between the single TM atom and B atom is present on the CO_2RR (Fig. 7). The TM-to-C and B-to-C π-back bonding contribute to the activation of the CO_2 molecules and CO intermediate. Enough electrons from the single TM atom and B atom can be injected into CO_2 and CO molecules through a direct bonding interaction. Therefore, the B-doping strategy efficiently controls the charge–orbital state of the coordination atom on the surface of $Ti_3C_2T_x$-MXene, alleviating remarkably the difficulty of activating CO_2 and CO molecules.

3.2.3. Subsequent protonation steps toward CO_2RR production. The excellent activation performance endows $TM@Ti_3C_2O_{2-x}B_x$ SACs with great potential for the CO_2RR. The outstanding CO activation performance can also help its further reduction reaction towards methane on $TM@Ti_3C_2O_{2-x}B_x$ SACs. Using the electronic potential energy surface (PES) as a baseline, we examine the subsequent protonation steps *via* the *COOH intermediate to form final product CH_4(g) in this section.

Fig. 8 shows the variation of the calculated free energy with the most favorable pathway for the reduction of CO_2 on $TM@Ti_3C_2O_{2-x}B_x$ SACs and the corresponding structures of the reaction intermediates are presented in Fig. S8 (ESI†). Owing to the excellent CO_2 activation performance of $TM@Ti_3C_2O_{2-x}B_x$, the hydrogenation of the adsorbed CO_2 to form *COOH is exothermic with a negative ΔG. The 3rd hydrogenation (H^+/e^-) reaction of *CO occurs, generating *CHO. *CO is more likely to undergo further reduction on all the $TM@Ti_3C_2O_{2-x}B_x$ because the ΔG of the protonation step ($*CO + H^+ + e^- \rightarrow *CHO$) is more negative than that of CO desorption. Therefore, we concluded that the production of CO can be effectively prohibited in the CO_2 reduction. The small ΔG of the 3rd hydrogenation also implies that the adsorbed *CO, which is generally regarded as the poison on metallic electrodes, is less likely to poison the active sites in our case.

For the subsequent elementary reaction steps passing through the CHO* intermediate to generate CH_4, it is worth mentioning that the desorption of CH_2O from $TM@Ti_3C_2O_{2-x}B_x$ is significantly endothermic due to their large negative adsorption energies (Table S2, ESI†), indicating that the production of methanol (CH_2O) can be effectively prevented during the reduction of CO_2 catalyzed by $TM@Ti_3C_2O_{2-x}B_x$. In addition, $*CH_3O$ is more likely to be further reduced to *O, releasing one CH_4 molecule on $TM@Ti_3C_2O_{2-x}B_x$ (TM is V, Cr or Mn). Therefore, the production of CH_3OH can be avoided effectively. For the case of $TM@Ti_3C_2O_{2-x}B_x$ (TM is Fe, Co or Ni), the desorption ΔG of CH_3OH is appreciably large so that the desorption of CH_3OH is difficult. After $*CH_3OH$ is formed on $TM@Ti_3C_2O_{2-x}B_x$, its C atom will be attacked by a proton to form CH_4(g) and *OH. This suggests that CH_4 is the primary reduction product on all the $TM@Ti_3C_2O_{2-x}B_x$ examined, indicating its great selectivity for catalyzing the CO_2 reduction to form CH_4 with excellent abilities to limit the production of CO(g), CH_2O(g), and CH_3OH(l).

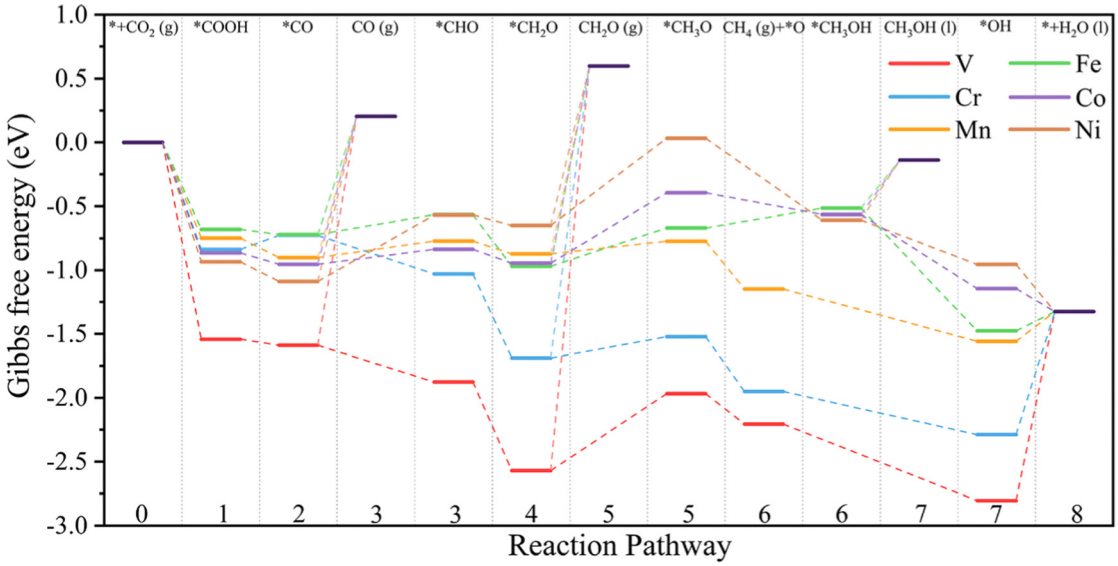

Fig. 8 Variation of the Gibbs free energy for the reduction reaction of CO_2 on TM@$Ti_3C_2O_{2-x}B_x$ (TM is V, Cr, Mn, Fe, Co or Ni,) at 0 V with RHE.

To assess the durability of TM@$Ti_3C_2O_{2-x}B_x$ SACs in practical application, we have further investigated the protonation of remaining *OH as well as the release of the adsorbed H_2O molecule (8th hydrogenation reaction). The results obtained show that the *OH on TM@$Ti_3C_2O_{2-x}B_x$ (TM is V or Cr) is harder to be removed; the uphill values of ΔG are 1.47 and 0.96 eV, respectively. The positive ΔG indicates that *OH is more likely to occupy active sites by forming TM–OH, which hinders the next CO_2 reduction process. For other TM@$Ti_3C_2O_{2-x}B_x$ (TM is Mn, Fe, Co or Ni), the formation of *CHO ($*CO + H^+ + e^- = *CHO$) and *CH_3O ($*CH_2O + H^+ + e^- = *CH_3O$) is both endothermic and the rest of the elementary steps are exothermic.

Except Mn@$Ti_3C_2O_{2-x}B_x$, the uphill value of ΔG for the formation of *CH_3O on TM@$Ti_3C_2O_{2-x}B_x$ (TM is Fe, Co or Ni) is larger than that for the formation of *CHO. Therefore, the formation of *CHO and *CH_3O is the potential-determining step (PDS) for Mn@$Ti_3C_2O_{2-x}B_x$ and TM@$Ti_3C_2O_{2-x}B_x$ (TM is Fe, Co or Ni), respectively. The PDS and the values of U_L predicted by DFT are summarized in Table 2. Based on the U_L calculated from the primary PDS, it can be inferred that Mn@$Ti_3C_2O_{2-x}B$ and Fe@$Ti_3C_2O_{2-x}B$ have a higher activity for CH_4 production, where their limiting potentials are 0.13 and 0.3 V, respectively, lower than those of other TM@$Ti_3C_2O_{2-x}B_x$.

Table 2 DFT-predicted potential determining steps (PDSs), U_L values, and possible products on TM@$Ti_3C_2O_{2-x}B_x$

Catalyst	Potential determining step	U_L (V)	Production
V@$Ti_3C_2O_{2-x}B_x$	$*OH + H^+ + e^- \rightarrow H_2O$ (l)	1.47	CH_4
Cr@$Ti_3C_2O_{2-x}B_x$	$*OH + H^+ + e^- \rightarrow H_2O$ (l)	0.96	CH_4
Mn@$Ti_3C_2O_{2-x}B_x$	$*CO + H^+ + e^- \rightarrow *CHO$	0.13	CH_4
Fe@$Ti_3C_2O_{2-x}B_x$	$*CH_2O + H^+ + e^- \rightarrow *CH_3O$	0.30	CH_4
Co@$Ti_3C_2O_{2-x}B_x$	$*CH_2O + H^+ + e^- \rightarrow *CH_3O$	0.55	CH_4
Ni@$Ti_3C_2O_{2-x}B_x$	$*CH_2O + H^+ + e^- \rightarrow *CH_3O$	0.68	CH_4

We conclude that Mn@$Ti_3C_2O_{2-x}B_x$ and Fe@$Ti_3C_2O_{2-x}B_x$ have a remarkable selectivity and activity for the production of CH_4(g). Considering the effect of the presence of water under real reaction conditions, we calculated the free energy diagram of the initial screening for Mn@$Ti_3C_2O_{2-x}B$ and Fe@$Ti_3C_2O_{2-x}B$ in the implicit solvent model using VASPsol (Fig. 9a and b). Notably, the levels of U_L for Mn@$Ti_3C_2O_{2-x}B$ and Fe@$Ti_3C_2O_{2-x}B$ increased to 0.51 and 0.40 V, respectively. The overpotential of Fe@$Ti_3C_2O_{2-x}B$ (0.40 V) suggests that it can be a promising CO_2RR catalyst for producing CH_4. This level of limiting potentials is comparable or lower than those of the widely employed transition metal-based CO_2RR electrocatalysts[8,14,80] and other bimetallic electrocatalysts work on CO_2 conversion to CH_4 (Table S3, ESI†).

3.3. Stability of Fe@$Ti_3C_2O_{2-x}B_x$ in solution and competition between the CO_2RR and the HER

Apart from CO_2 adsorption, the competitive adsorption of CO_2RR and H on each active center is also a significant factor affecting CO_2RR performance. The free energy of hydrogen adsorption (ΔG_H) provides a measure for evaluating HER activity. A material is an optimal HER electrocatalyst if its ΔG_H value is close to zero. However, a highly negative ΔG_H indicates the excessively stable adsorption of H on the active sites, thereby preventing the CO_2RR. Therefore, active sites with a large ΔG_H are desirable for CO_2RR electrocatalysts. Assuming a Volmer and Tafel mechanism, we calculated the ΔG for the formation of *COOH ($* + CO_2 + H^+ + e^- \rightarrow *COOH$) and that for the formation of *H ($H^+ + e^- \rightarrow *H$) in the HER. According to Brønsted–Evans–Polanyi (BEP) relations, a reaction with a more negative ΔG is expected to encounter a smaller reaction barrier and, therefore, is more favored to occur.

The adsorption sites for the H atom mainly locate on the bridge site between the TM and B atoms on Fe@$Ti_3C_2O_{2-x}B_x$ (Fig. 9c). The calculated ΔG_H of Fe@$Ti_3C_2O_{2-x}B_x$ is −0.48 eV,

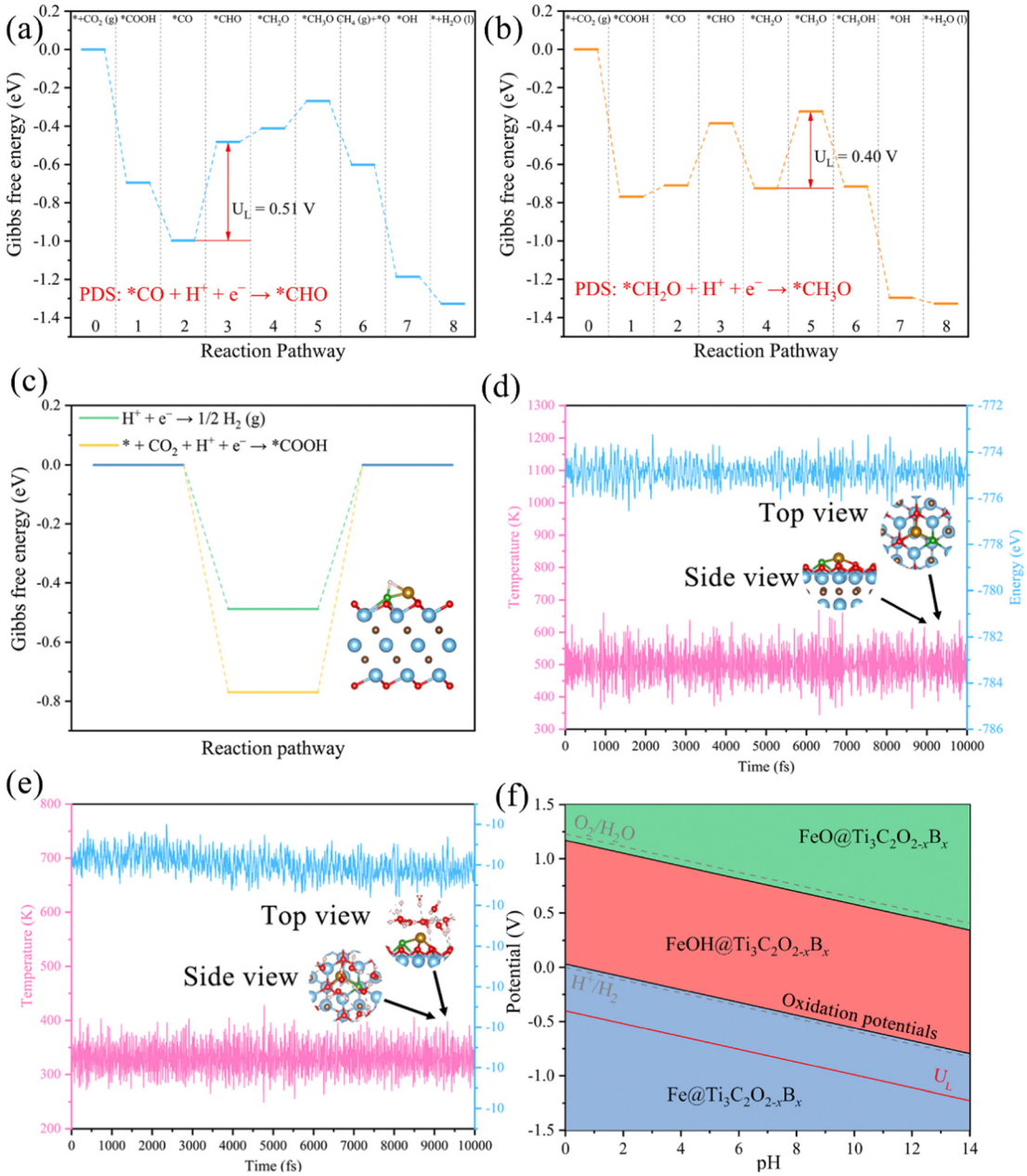

Fig. 9 Free energy diagrams of the CO_2RR on (a) $Mn@Ti_3C_2O_{2-x}B$ and (b) $Fe@Ti_3C_2O_{2-x}B$ after taking into account of solvation effects. (c) Variation of the Gibbs free energy changes (ΔG) for the first protonation step of the CO_2RR with HER. Inset: the optimized geometric structures of H adsorbed on $Fe@Ti_3C_2O_{2-x}B_x$. (d) Variations of energy and temperature with the AIMD simulation time for $Fe@Ti_3C_2O_{2-x}B$, where the AIMD simulation lasts for 10 ps at 500 K. (e) Variations of energy and temperature with the AIMD simulation time for $Fe@Ti_3C_2O_{2-x}B$, an explicit solvent model is used to simulate the acidic aqueous solution. The AIMD simulation lasts for 10 ps at 330 K. (f) Calculated Pourbaix diagram of $Fe@Ti_3C_2O_{2-x}B$. Gray dashed lines denote the water redox potentials.

which is more positive than the ΔG_{*COOH} of the CO_2RR (Fig. 9c). This suggests that $Fe@Ti_3C_2O_{2-x}B_x$ contains inactive sites for the HER with a $|\Delta G_H|$ of around 0.5 eV and exhibits a higher selectivity toward the CO_2RR than the HER.

To assess the durability of MXene catalysts in practical applications, we investigated the stability of $Fe@Ti_3C_2O_{2-x}B_x$ *via* AIMD simulations. As seen in Fig. 9d, both the total energy and the temperature oscillate near the initial conditions and the geometric structures of $Fe@Ti_3C_2O_{2-x}B_x$ are preserved well within 10 ps. An explicit solvent model is also applied to simulate the solution environment, and AIMD simulations are performed to study the thermal stability of $Fe@Ti_3C_2O_{2-x}B_x$ in a solution at 330 K for 10 ns.

The results obtained reveal that the structure of $Fe@Ti_3C_2O_{2-x}B_x$ can remain stable in an aqueous solution (Fig. 9e). Therefore, it can be inferred that $Fe@Ti_3C_2O_{2-x}B_x$ can serve as an efficient CO_2RR electrocatalyst under ambient conditions with a high stability. Further analysis of the Pourbaix diagram

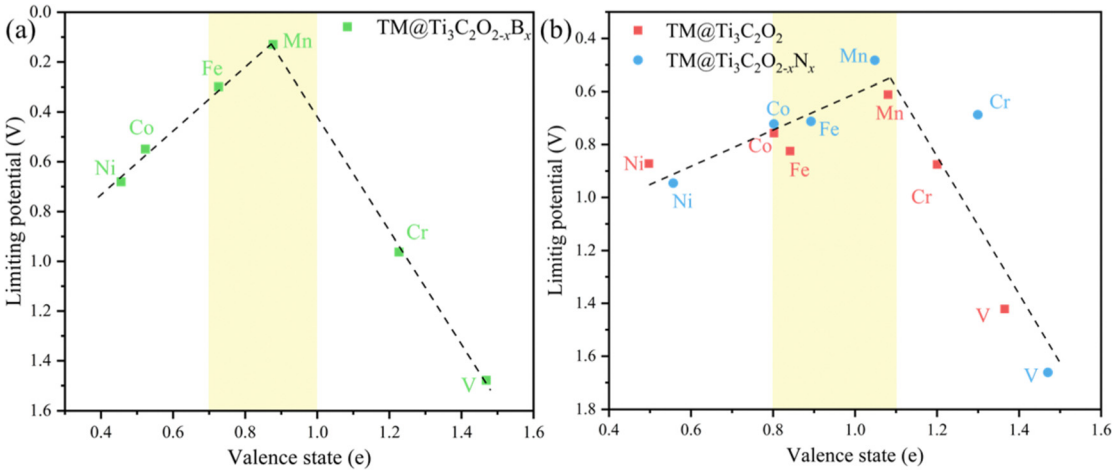

Fig. 10 The limiting potential as a function of the valence state of TM atoms fixed on (a) $Ti_3C_2O_{2-x}B_x$ and (b) $Ti_3C_2O_2$, $Ti_3C_2O_{2-x}N_x$.

of Fe@$Ti_3C_2O_{2-x}B_x$ (Fig. 9f) has also been carried out. It is a useful tool to identify the stable state of catalysts in water as a function of pH and applied potential. The oxidation potential of Fe@$Ti_3C_2O_{2-x}B_x$ at pH 0 (black line) is less negative than the U_L value of Fe@$Ti_3C_2O_{2-x}B_x$ (red line), indicating that Fe@$Ti_3C_2O_{2-x}B_x$ could possess superior electrochemical stability against surface oxidation under working conditions.

3.4. An activity descriptor for CO_2 reduction on $Ti_3C_2T_x$-based SACs

It is beneficial to search an activity descriptor to establish a "volcano" relationship on catalytic behaviors so that we can further roughly estimate the effect of other potential dopants on the CO_2RR performance. It is generally agreed that the electronic structures of catalytic centers would greatly influence the electron transfer and reaction energy in catalytic processes. Pan and coworkers have found that the valence state of TMs could be used as an activity descriptor, wherefore the limiting potential towards different products as a function of the valence state of TMs[81] because the TM atoms can provide both empty d orbitals to accept electrons to form a coordination bond and lone electrons to form a covalent bond.[82] Hence, the valence state of TMs would directly influence the bonding strength with the intermediates.

The valence state of different TM atoms is defined as the number of electrons transferred from the TM atom to the substrate. Using the valence state of TMs as the descriptor, we find that a volcano trend is observed for TM@$Ti_3C_2O_{2-x}B_x$ (Fig. 10a), meaning this descriptor is possible to estimate the catalytic performance of the TM@$Ti_3C_2O_2$ system. Therefore, a brief calculation of N-doped $Ti_3C_2O_2$-based SACs (TM@$Ti_3C_2O_{2-x}N_x$) is carried out to verify the accuracy of this descriptor. The adsorption configuration of CO_2 and CO on TM@$Ti_3C_2O_{2-x}N_x$ (Fig. S9, ESI†) indicates that the nitrogen atom is only used as the coordination atom to control the electronic structure of the TM. Generally, the potential-limiting step of CO_2 reduction is the hydrogenation of *COOH to *CO or the hydrogenation of *CO to *CHO.[83,84] As for the TM@$Ti_3C_2O_2$ system studied in our work, $*OH + H^+ + e^- \rightarrow H_2O(l)$ is the potential-limiting step on V@$Ti_3C_2O_2$ and Cr@$Ti_3C_2O_2$. Hence, we have calculated these key reaction steps on TM@$Ti_3C_2O_{2-x}N_x$ and chosen the step with the largest reaction energy barrier as the potential-limiting step.

The result shows that a volcano trend is observed with the optimal scope of the valence state ranging from ~0.8 e to ~1.1 e (Fig. 10b). We can see that the optimal scope of the valence state is different between TM@$Ti_3C_2O_{2-x}B_x$ and TM@$Ti_3C_2O_2$ (TM@$Ti_3C_2O_{2-x}B_x$). Because the boron atom can participate in CO_2 reduction, the scaling relations between the adsorption strength of reaction intermediates have been broken. This simple descriptor well explains the catalytic performance of the TM@$Ti_3C_2O_2$ and doped TM@$Ti_3C_2O_2$ SACs and suggests that a certain moderate degree of electron transfer from TM atoms to the substrate will be expected to promote the overall catalytic activity. Before using this descriptor, we need to determine whether the coordination atoms participate in the reaction to ensure that the same linear relationship exists. Moreover, this descriptor can only roughly estimate the CO_2RR performance of catalysts. A series of subsequent tests, such as the competition test, stability test and solvation effect should be considered to further screening out the most suitable catalysts.

4. Conclusions

In summary, by applying well-defined first-principles calculations, we have investigated the single-atom catalysts of $Ti_3C_2O_{2-x}B_x$ monolayers for CO_2 electrochemical reduction reactions. The results obtained suggest that the B atom not only serves as the coordination atom to anchor single TM atoms but also plays an important role in the CO_2 electrochemical reduction process. The strategy of doping B regulates the charge–orbit distribution of the surface functional groups of $Ti_3C_2O_2$. By analyzing charge transfer and DOS calculation results, the combined effect of the single TM atom and the adjacent B atom in $Ti_3C_2O_{2-x}B_x$ on the CO_2RR has been

demystified. The empty orbitals in B atom hybridization help it in gaining more electrons from single TM atoms, forming strong-polarized covalent TM–B bonds, which is beneficial for anchoring single TM atoms on the $Ti_3C_2O_2$ surface. The electrons provided by the occupied orbitals in B atom hybridization are effectively transferred to the π-antibonding orbitals of CO_2 and CO, thereby helping single TM atoms to activate the CO_2 molecules and *CO intermediate. Especially, the activation of the *CO intermediate induced by the combined effect effectively lowers the reaction energy barrier of the protonation step of *CO, facilitating further CO reduction towards CH_4.

Our results also demonstrated that the activated CO_2 can be further reduced to CH_4 by TM@$Ti_3C_2O_{2-x}B_x$, in which Fe@$Ti_3C_2O_{2-x}B_x$ exhibits a better catalytic efficiency with a low limiting potential of ~0.40 V. In addition, AIMD calculations reveal that Fe@$Ti_3C_2O_{2-x}B_x$ has a high stability. Inspired by the successful preparation of Ru@$Ti_3C_2O_{2-x}B_x$ SACs,[55] the practical application of Fe@$Ti_3C_2O_{2-x}B_x$ in CO_2 capture and reduction can be reasonably anticipated in the near future. We conclude that our work provides atomic-level insights into the combined effect between the embedded single metal atom and the innate atom in a substrate and provides an important strategy for the design of MXenes as novel CO_2RR catalysts.

Conflicts of interest

There are no conflicts to declare.

Acknowledgements

This work was supported by Guangdong Basic and Applied Basic Research Foundation (No. 2022A1515011303), the Central Government Guides Local Science and Technology Development Funds to Freely Explore Basic Research Projects (2021Szvup106), the Natural Science Fund for Distinguished Young Scholars of Hubei Province (No. 2020CFA087), the Basic Research Program of Shenzhen (No. JCYJ20190809120015163); and the Fundamental Research Funds for the Central Universities.

References

1 Ş. Kılkış, G. Krajačić, N. Duić, M. A. Rosen and M. D. A. Al-Nimr, *Energy Convers. Manage.*, 2020, **225**, 113410.
2 D. Guan, J. Meng, D. M. Reiner, N. Zhang, Y. Shan, Z. Mi, S. Shao, Z. Liu, Q. Zhang and S. J. Davis, *Nat. Geosci.*, 2018, **11**, 551–555.
3 Z. Chu, M. Cheng and N. N. Yu, *Technol. Forecase. Soc.*, 2021, **172**, 121037.
4 X. Zhao, Y. Shang and M. Song, *Socio-Econ. Plan. Sci.*, 2020, **72**, 100757.
5 X. Zhao, X. Ma, B. Chen, Y. Shang and M. Song, *Resour., Conserv. Recycl.*, 2022, **176**, 105959.
6 M. Salvia, D. Reckien, F. Pietrapertosa, P. Eckersley, N.-A. Spyridaki, A. Krook-Riekkola, M. Olazabal, S. De Gregorio Hurtado, S. G. Simoes, D. Geneletti, V. Viguié, P. A. Fokaides, B. I. Ioannou, A. Flamos, M. S. Csete, A. Buzasi, H. Orru, C. de Boer, A. Foley, K. Rižnar, M. Matosović, M. V. Balzan, M. Smigaj, V. Baštáková, E. Streberova, N. B. Šel, L. Coste, L. Tardieu, C. Altenburg, E. K. Lorencová, K. Orru, A. Wejs, E. Feliu, J. M. Church, S. Grafakos, S. Vasilie, I. Paspaldzhiev and O. Heidrich, *Renewable Sustainable Energy Rev.*, 2021, **135**, 110253.
7 Z. Liu, Z. Deng, G. He, H. Wang, X. Zhang, J. Lin, Y. Qi and X. Liang, *Nat. Rev. Earth Environ.*, 2022, **3**, 141–155.
8 M. M. Ayyub and C. N. R. Rao, *Mater. Horiz.*, 2021, **8**, 2420–2443.
9 Z. Sun, T. Ma, H. Tao, Q. Fan and B. Han, *Chem*, 2017, **3**, 560–587.
10 L. Dietz, S. Piccinin and M. Maestri, *J. Phys. Chem. C*, 2015, **119**, 4959–4966.
11 X. Li, S. Wang, L. Li, X. Zu, Y. Sun and Y. Xie, *Acc. Chem. Res.*, 2020, **53**, 2964–2974.
12 D. W. DeWulf, T. Jin and A. J. Bard, *J. Electrochem. Soc.*, 1989, **136**, 1686.
13 Y. Hori, in *Modern Aspects of Electrochemistry*, ed. C. G. Vayenas, R. E. White and M. E. Gamboa-Aldeco, Springer New York, New York, NY, 2008, pp. 89–189, DOI: 10.1007/978-0-387-49489-0_3.
14 A. A. Peterson, F. Abild-Pedersen, F. Studt, J. Rossmeisl and J. K. Nørskov, *Energy Environ. Sci.*, 2010, **3**, 1311–1315.
15 W. Chen, J. Cao, W. Fu, J. Zhang, G. Qian, J. Yang, D. Chen, X. Zhou, W. Yuan and X. Duan, *Angew. Chem., Int. Ed.*, 2022, **61**, e202200190.
16 Y.-J. Zhang, V. Sethuraman, R. Michalsky and A. A. Peterson, *ACS Catal.*, 2014, **4**, 3742–3748.
17 X. Chen, L. P. Granda-Marulanda, I. T. McCrum and M. T. M. Koper, *Nat. Commun.*, 2022, **13**, 38.
18 J. Albo and A. Irabien, *J. Catal.*, 2016, **343**, 232–239.
19 I. Merino-Garcia, J. Albo, J. Solla-Gullón, V. Montiel and A. Irabien, *J. CO2 Util.*, 2019, **31**, 135–142.
20 Y. Hori, A. Murata and R. Takahashi, *J. Chem. Soc., Faraday Trans. 1*, 1989, **85**, 2309–2326.
21 J. Albo, G. Beobide, P. Castaño and A. Irabien, *J. CO2 Util.*, 2017, **18**, 164–172.
22 J. Albo, A. Sáez, J. Solla-Gullón, V. Montiel and A. Irabien, *Appl. Catal., B*, 2015, **176–177**, 709–717.
23 J. Albo, D. Vallejo, G. Beobide, O. Castillo, P. Castaño and A. Irabien, *ChemSusChem*, 2017, **10**, 1100–1109.
24 M. Perfecto-Irigaray, J. Albo, G. Beobide, O. Castillo, A. Irabien and S. Pérez-Yáñez, *RSC Adv.*, 2018, **8**, 21092–21099.
25 I. Merino-Garcia, J. Albo, P. Krzywda, G. Mul and A. Irabien, *Catal. Today*, 2020, **346**, 34–39.
26 Q. Zhang and J. Guan, *Adv. Funct. Mater.*, 2020, **30**, 2000768.
27 M. Li, H. Wang, W. Luo, P. C. Sherrell, J. Chen and J. Yang, *Adv. Mater.*, 2020, **32**, 2001848.
28 R. Wang, G. Liu, S. K. Kim, K. H. Bowen and X. Zhang, *J. Energy Chem.*, 2021, **63**, 130–137.
29 N. Li, X. Wang, X. Lu, P. Zhang and W.-J. Ong, *Chem. – Eur. J.*, 2021, **27**, 17900–17909.

30 J. Fu, L. Zhu, K. Jiang, K. Liu, Z. Wang, X. Qiu, H. Li, J. Hu, H. Pan, Y.-R. Lu, T.-S. Chan and M. Liu, *Chem. Eng. J.*, 2021, **415**, 128982.
31 C. Ling, X. Niu, Q. Li, A. Du and J. Wang, *J. Am. Chem. Soc.*, 2018, **140**, 14161–14168.
32 H. Yin, L.-Y. Gan and P. Wang, *J. Mater. Chem. A*, 2020, **8**, 3910–3917.
33 M.-A. Légaré, G. Bélanger-Chabot, R. D. Dewhurst, E. Welz, I. Krummenacher, B. Engels and H. Braunschweig, *Science*, 2018, **359**, 896–900.
34 M. Qu, G. Qin, J. Fan, A. Du and Q. Sun, *Appl. Surf. Sci.*, 2021, **555**, 149652.
35 Y. Jiao, A. Du, Z. Zhu, V. Rudolph, G. Q. Lu and S. C. Smith, *Catal. Today*, 2011, **175**, 271–275.
36 S. Tang, X. Zhou, S. Zhang, X. Li, T. Yang, W. Hu, J. Jiang and Y. Luo, *ACS Appl. Mater. Interfaces*, 2019, **11**, 906–915.
37 X. Chen, W.-J. Ong, X. Zhao, P. Zhang and N. Li, *J. Energy Chem.*, 2021, **58**, 577–585.
38 S. Liu, M. Jin, J. Sun, Y. Qin, S. Gao, Y. Chen, S. Zhang, J. Luo and X. Liu, *Chem. Eng. J.*, 2022, **437**, 135294.
39 H. Xu, Y. Zhao, Q. Wang, G. He and H. Chen, *Coord. Chem. Rev.*, 2022, **451**, 214261.
40 J. Li, Q. Guan, H. Wu, W. Liu, Y. Lin, Z. Sun, X. Ye, X. Zheng, H. Pan, J. Zhu, S. Chen, W. Zhang, S. Wei and J. Lu, *J. Am. Chem. Soc.*, 2019, **141**, 14515–14519.
41 N. Li, X. Chen, W.-J. Ong, D. R. MacFarlane, X. Zhao, A. K. Cheetham and C. Sun, *ACS Nano*, 2017, **11**, 10825–10833.
42 J. Peng, X. Chen, W.-J. Ong, X. Zhao and N. Li, *Chem*, 2019, **5**, 18–50.
43 R. A. Soomro, S. Jawaid, Q. Zhu, Z. Abbas and B. Xu, *Chin. Chem. Lett.*, 2020, **31**, 922–930.
44 Y. Dong, H. Shi and Z.-S. Wu, *Adv. Funct. Mater.*, 2020, **30**, 2000706.
45 B. Huang, N. Li, W.-J. Ong and N. Zhou, *J. Mater. Chem. A*, 2019, **7**, 27620–27631.
46 Y. Meng, J.-X. Liang, C. Zhu, C.-Q. Xu and J. Li, *Sci. China Mater.*, 2022, **65**, 1303–1312.
47 G. Chen, M. Ding, K. Zhang, Z. Shen, Y. Wang, J. Ma, A. Wang, Y. Li and H. Xu, *ChemSusChem*, 2022, **15**, e202102352.
48 M. Zhang, C. Lai, B. Li, S. Liu, D. Huang, F. Xu, X. Liu, L. Qin, Y. Fu, L. Li, H. Yi and L. Chen, *Small*, 2021, **17**, 2007113.
49 Y. Cui, Z. Cao, Y. Zhang, H. Chen, J. Gu, Z. Du, Y. Shi, B. Li and S. Yang, *Small Sci.*, 2021, **1**, 2100017.
50 D. Zhao, Z. Chen, W. Yang, S. Liu, X. Zhang, Y. Yu, W.-C. Cheong, L. Zheng, F. Ren, G. Ying, X. Cao, D. Wang, Q. Peng, G. Wang and C. Chen, *J. Am. Chem. Soc.*, 2019, **141**, 4086–4093.
51 Q. Zhao, C. Zhang, R. Hu, Z. Du, J. Gu, Y. Cui, X. Chen, W. Xu, Z. Cheng, S. Li, B. Li, Y. Liu, W. Chen, C. Liu, J. Shang, L. Song and S. Yang, *ACS Nano*, 2021, **15**, 4927–4936.
52 W. Lin, Y.-R. Lu, W. Peng, M. Luo, T.-S. Chan and Y. Tan, *J. Mater. Chem. A*, 2022, **10**, 9878–9885.
53 H. Liu, Z. Hu, Q. Liu, P. Sun, Y. Wang, S. Chou, Z. Hu and Z. Zhang, *J. Mater. Chem. A*, 2020, **8**, 24710–24717.
54 Z. Chen, J. Cao, X. Wu, D. Cai, M. Luo, S. Xing, X. Wen, Y. Chen, Y. Jin, D. Chen, Y. Cao, L. Wang, X. Xiong and B. Yu, *ACS Appl. Mater. Interfaces*, 2022, **14**, 12223–12233.
55 M. Bat-Erdene, M. Batmunkh, B. Sainbileg, M. Hayashi, A. S. R. Bati, J. Qin, H. Zhao, Y. L. Zhong and J. G. Shapter, *Small*, 2021, **17**, 2102218.
56 N. Li, J. Peng, Z. Shi, P. Zhang and X. Li, *Chin. J. Catal.*, 2022, **43**, 1906–1917.
57 J. Hafner, *J. Comput. Chem.*, 2008, **29**, 2044–2078.
58 J. P. Perdew, K. Burke and M. Ernzerhof, *Phys. Rev. Lett.*, 1996, **77**, 3865–3868.
59 P. E. Blöchl, *Phys. Rev. B: Condens. Matter Mater. Phys.*, 1994, **50**, 17953–17979.
60 S. Grimme, J. Antony, S. Ehrlich and H. Krieg, *J. Chem. Phys.*, 2010, **132**, 154104.
61 E. Sanville, S. D. Kenny, R. Smith and G. Henkelman, *J. Comput. Chem.*, 2007, **28**, 899–908.
62 K. Momma and F. Izumi, *J. Appl. Crystallogr.*, 2011, **44**, 1272–1276.
63 C. M. Gray, K. Saravanan, G. Wang and J. A. Keith, *Mol. Simul.*, 2017, **43**, 420–427.
64 F. Calle-Vallejo, R. F. de Morais, F. Illas, D. Loffreda and P. Sautet, *J. Phys. Chem. C*, 2019, **123**, 5578–5582.
65 Q. Zhang and A. Asthagiri, *Catal. Today*, 2019, **323**, 35–43.
66 L. Li, B. Li, Q. Guo and B. Li, *J. Phys. Chem. C*, 2019, **123**, 14501–14507.
67 H. Dong, C. Liu, Y. Li and D.-E. Jiang, *Nanoscale*, 2019, **11**, 11351–11359.
68 J. K. Nørskov, J. Rossmeisl, A. Logadottir, L. Lindqvist, J. R. Kitchin, T. Bligaard and H. Jónsson, *J. Phys. Chem. B*, 2004, **108**, 17886–17892.
69 F. Calle-Vallejo, J. I. Martínez, J. M. García-Lastra, M. Mogensen and J. Rossmeisl, *Angew. Chem., Int. Ed.*, 2010, **49**, 7699–7701.
70 Y. Li, H. Su, S. H. Chan and Q. Sun, *ACS Catal.*, 2015, **5**, 6658–6664.
71 D. R. Lide, *CRC handbook of chemistry and physics*, CRC Press, 2004.
72 Y. Gao, Y. Cao, Y. Gu, H. Zhuo, G. Zhuang, S. Deng, X. Zhong, Z. Wei, J. Chen, X. Pan and J.-G. Wang, *Appl. Surf. Sci.*, 2019, **465**, 911–918.
73 P. Li, J. Zhu, A. D. Handoko, R. Zhang, H. Wang, D. Legut, X. Wen, Z. Fu, Z. W. Seh and Q. Zhang, *J. Mater. Chem. A*, 2018, **6**, 4271–4278.
74 C. Guo, T. Zhang, X. Liang, X. Deng, W. Guo, Z. Wang, X. Lu and C.-M. L. Wu, *Appl. Surf. Sci.*, 2020, **533**, 147466.
75 X. Cui, W. An, X. Liu, H. Wang, Y. Men and J. Wang, *Nanoscale*, 2018, **10**, 15262–15272.
76 M. Wang, L. Kong, X. Lu and C.-M. Lawrence Wu, *J. Mater. Chem. A*, 2022, **10**, 9048–9058.
77 T. Liu, G. Wang and X. Bao, *J. Phys. Chem. C*, 2021, **125**, 26013–26020.

78 A. Föhlisch, M. Nyberg, P. Bennich, L. Triguero, J. Hasselström, O. Karis, L. G. M. Pettersson and A. Nilsson, *J. Chem. Phys.*, 2000, **112**, 1946–1958.
79 K. M. Gameel, I. M. Sharafeldin, A. U. Abourayya, A. H. Biby and N. K. Allam, *Phys. Chem. Chem. Phys.*, 2018, **20**, 25892–25900.
80 X. Hong, K. Chan, C. Tsai and J. K. Nørskov, *ACS Catal.*, 2016, **6**, 4428–4437.
81 S. Zheng, C. Zuo, X. Liang, S. Li and F. Pan, *J. Energy Chem.*, 2021, **56**, 444–448.
82 L. Gong, D. Zhang, C.-Y. Lin, Y. Zhu, Y. Shen, J. Zhang, X. Han, L. Zhang and Z. Xia, *Adv. Energy Mater.*, 2019, **9**, 1902625.
83 Y. Ouyang, L. Shi, X. Bai, Q. Li and J. Wang, *Chem. Sci.*, 2020, **11**, 1807–1813.
84 C. Li, X. Liu, F. Xu, D. Wu, H. Xu and G. Fan, *Electrochim. Acta*, 2022, **426**, 140764.

